

Finite element analysis of the pressure-induced deformation of Schlemm's canal endothelial cells

Rocio Vargas-Pinto, Julia Lai, Haiyan Gong, C. Ross Ethier & Mark Johnson

Biomechanics and Modeling in Mechanobiology

ISSN 1617-7959

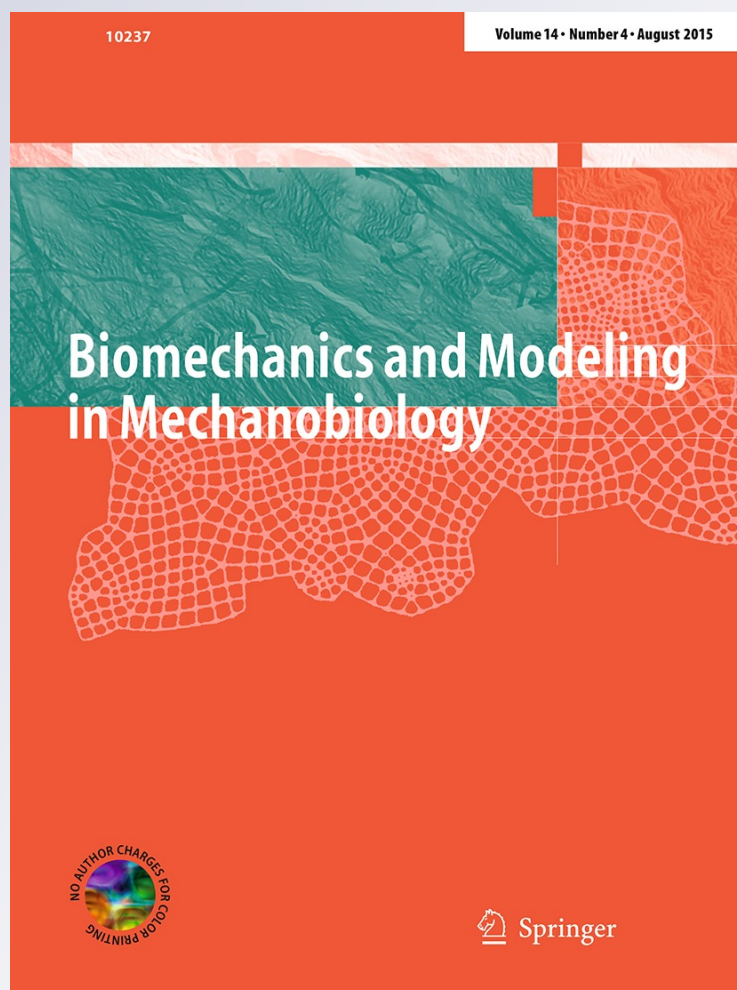
Volume 14

Number 4

Biomech Model Mechanobiol (2015)

14:851-863

DOI 10.1007/s10237-014-0640-2



Your article is protected by copyright and all rights are held exclusively by Springer-Verlag Berlin Heidelberg. This e-offprint is for personal use only and shall not be self-archived in electronic repositories. If you wish to self-archive your article, please use the accepted manuscript version for posting on your own website. You may further deposit the accepted manuscript version in any repository, provided it is only made publicly available 12 months after official publication or later and provided acknowledgement is given to the original source of publication and a link is inserted to the published article on Springer's website. The link must be accompanied by the following text: "The final publication is available at link.springer.com".

Finite element analysis of the pressure-induced deformation of Schlemm's canal endothelial cells

Rocio Vargas-Pinto · Julia Lai · Haiyan Gong ·
C. Ross Ethier · Mark Johnson

Received: 29 August 2014 / Accepted: 5 December 2014 / Published online: 17 December 2014
© Springer-Verlag Berlin Heidelberg 2014

Abstract The endothelial cells lining the inner wall of Schlemm's canal (SC) in the eye are relatively unique in that they support a basal-to-apical pressure gradient that causes these cells to deform, creating giant vacuoles and transendothelial pores through which the aqueous humor flows. Glaucoma is associated with an increased resistance to this flow. We used finite element modeling and estimates of cell modulus made using atomic force microscopy to characterize the pressure-induced deformation of SC cells and to estimate the maximum pressure drop that SC cells can support. We examined the effects of cell geometry, cell stiffness,

and the contribution of the cell cortex to support the pressure-generated load. We found that the maximum strain generated by this loading occurs at the points of cell–substrate attachment and that the cortex of the cells bears nearly all of this load. The ability of these cells to support a significant transcellular pressure drop is extremely limited (on the order of 5 mmHg or less) unless these cells either stiffen very considerably with increasing deformation or have substantial attachments to their substratum away from their periphery. This puts limits on the flow resistance that this layer can generate, which has implications regarding the site where the bulk of the flow resistance is generated in healthy and glaucomatous eyes.

Electronic supplementary material The online version of this article (doi:[10.1007/s10237-014-0640-2](https://doi.org/10.1007/s10237-014-0640-2)) contains supplementary material, which is available to authorized users.

R. Vargas-Pinto
Department of Biomedical Engineering, Northwestern University,
Evanston, IL 60208, USA

J. Lai · H. Gong
Departments of Anatomy and Neurobiology, Boston University
School of Medicine, Boston, MA 02118, USA

J. Lai · H. Gong
Department of Ophthalmology, Boston University
School of Medicine, Boston, MA 02118, USA

C. R. Ethier
Wallace H. Coulter Department of Biomedical Engineering,
Georgia Institute of Technology, Atlanta, GA 30332, USA

C. R. Ethier
Departments of Biomedical Engineering and Ophthalmology,
Emory University, Atlanta, GA 30322, USA

M. Johnson (✉)
Departments of Biomedical Engineering, Mechanical Engineering
and Ophthalmology, Northwestern University,
Evanston, IL 60208, USA
e-mail: m-johnson2@northwestern.edu

Keywords Aqueous humor outflow resistance · Strain ·
Cell cortex · Glaucoma

1 Introduction

Primary open-angle glaucoma is a potentially blinding disease frequently associated with an increased intraocular pressure, which in turn is caused by an elevated resistance to the drainage of aqueous humor (Grant 1951) from the eye. The cause of this increased resistance remains unknown, and its discovery has been hindered by the limited understanding of the locus and mechanism of the generation of aqueous outflow resistance. Experimental evidence suggests that the bulk of the outflow resistance in healthy, and likely also in glaucomatous, eyes is located in a narrow region consisting of the inner wall endothelium of Schlemm's canal (SC), its basement membrane, and adjacent juxtacanalicular connective tissue (JCT) (Johnson 2006). Figure 1 shows the location of these structures in the eye and the direction of flow of aqueous humor.

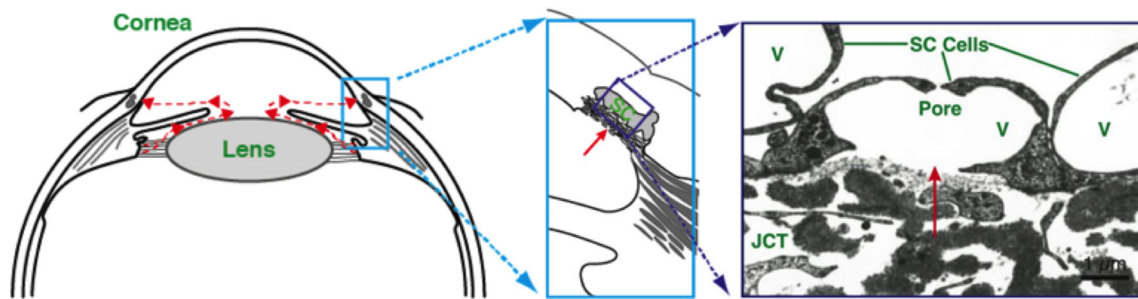


Fig. 1 Aqueous humor flow pathway. *Left* schematic of anterior segment of eye showing the direction of aqueous humor flow in red. *Center* enlargement of the iris–cornea angle (boxed region in left panel) to show the conventional outflow pathway. *Right* Transmission electron micro-

graph of endothelial cells forming the inner wall of SC; aqueous humor crosses the endothelium through pores to enter the lumen of SC. V, giant vacuoles; JCT, juxtacanalicular connective tissue (Overby et al. 2014)

Schlemm's canal cells are subject to a relatively unique biomechanical environment. Unlike vascular endothelial cells exposed to an apical-to-basal pressure gradient that is supported by their basement membrane, SC cells are subject to a basal-to-apical pressure gradient that pushes cells away from their supporting basement membrane. As a result, SC cells undergo very large deformations and create structures known as giant vacuoles (Brilakis and Johnson 2001; Grierson and Lee 1977); these deformations are thought to lead to pore formation in these cells, through which the aqueous humor flows (Ethier et al. 1998; Johnson et al. 1990). Because the density of these pores has been observed to be reduced in glaucomatous eyes (Allingham et al. 1992; Johnson et al. 2002), there is a need to better understand the biomechanics of the inner wall of SC.

Here, we describe the use of serial block-face scanning electron microscopy (SBSEM) and finite element modeling (FEM) combined with atomic force microscopy (AFM) measurements of the modulus of SC cells (Vargas-Pinto et al. 2013) to characterize the effects of cell geometry, cell stiffness, and the contribution of the cell cortex to the pressure-generated deformation of SC cells; we also estimate the maximum pressure drop that these cells can support. By establishing this upper bound, we can determine whether the inner wall endothelium of SC can be reasonably assumed to support a significant fraction of the entire pressure drop across the conventional outflow pathway.

2 Methods

2.1 Imaging of SC cells

Two human donor eyes with no known history of eye disease (age 69 and 70 years) were received from National Disease Research Interchange (Philadelphia, PA) within 24 h post-mortem. Radial and frontal tissue samples of the trabecular meshwork were cut and fixed with 2.5 % glutaraldehyde and 4 % paraformaldehyde in a 0.1-M sodium cacodylate buffer.

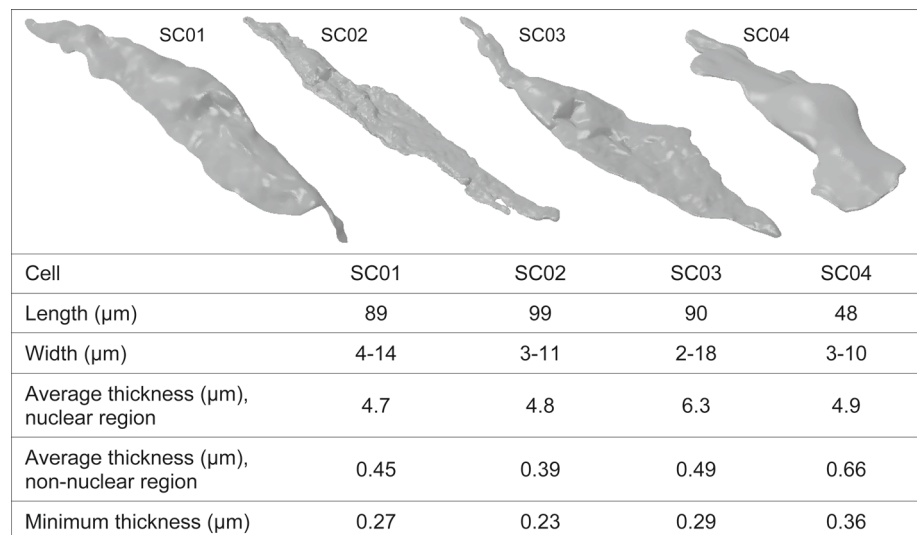
The fixed tissues were stained with tannic acid and then stained with osmium-ferrocyanide, followed by tetracarbohydrazide treatment, and then further stained with aqueous osmium tetroxide. Tissues were then incubated in saturated aqueous uranyl acetate, followed by Walton's lead aspartate (Deerinck et al. 2010). Following this, tissues were dehydrated and embedded in Epon.

SBSEM image data sets were acquired at Renovo Neural Inc. (Cleveland, OH). A sample image is given in Online Resource 1. The tissue blocks were mounted, examined, and sectioned in a Zeiss Sigma VP scanning electron microscope equipped with a Gatan 3View in-chamber ultramicrotome stage with low-kV backscattered electron detectors optimized for 3View systems. The inner wall endothelium of SC in each sample block was initially identified, and the regions of interest were chosen to include small portion of lumen of SC, inner wall endothelium of SC, and the underlying JCT. The first sample block was sectioned longitudinally along the longer axis of SC. A series of 500 EM images in a field size of $204.80 \times 61.40 \mu\text{m}$ were acquired at 2.25 kV with a resolution of 10 nm per pixel and 100 nm per slice. Five inner wall endothelial cells were captured from this data set. However, due to the great cell length, the limited field size could only capture one endothelial cell (SC04), while the other four cells were partially out of field. To ensure capture of the full length of SC cells while maintaining similar field size and resolution, cross sections along the shorter axis of SC were cut in the second sample block. Each image obtained from this block showed a transverse view of the cell. A series of 1001 EM images in a field size of $53.30 \times 31.98 \mu\text{m}$ were acquired at 1.5 kV, with a resolution of 10.41 nm per pixel and 150 nm per slice. Three inner wall endothelial cells were captured in full length from the second data set.

2.2 Geometry reconstruction

Based on the microscopic images, 4 cell-specific geometries were created: SC01, SC02, SC03, and SC04 (Fig. 2). Due to

Fig. 2 SC cell geometries as reconstructed from SBSEM images



the smaller number of images used to reconstruct SC04, the resulting geometry was smoother than those of the other 3 cells. Briefly, the series of microscopic images from each cell were registered and resized as necessary using ImageJ/FIJI software (<http://fiji.sc/>). Cell boundaries were traced using Reconstruct software (Fiala 2005) as previously described (Müller-Reichert et al. 2010).

The coordinates of the cell boundaries were then imported as a point cloud into Geomagic Studio 2014 (3D Systems, Rock Hill, SC) software in order to create a three-dimensional geometry in a format that was compatible with the finite element analysis software. Using Geomagic, the point cloud (coordinates taken from microscopic images) for each cell was smoothed and then converted to nonuniform rational basis spline surfaces.

SC cells were modeled as homogeneous materials, and the contribution of the cell cortex was separately examined by modeling one of the cells (SC04) as having two components with different material properties: a stiff cortex (Vargas-Pinto et al. 2013), and the rest of the cell, which we here refer to as the cytoplasm.

To create the geometry for cells with a stiff cortex, Geomagic was used to create a new, interior surface that was either 100 or 200 nm away from the original (exterior) surface created from the point cloud for SC04. The new interior surface was generated by projecting the vertices of the original surface in the normal direction. The geometry of the cell cortex was created by combining the interior (new) and original (exterior) surfaces, while only the interior (new) surface was used to create the geometry of the cytoplasm. The resulting geometry for the cell cortex had a uniform thickness throughout.

The thickness of the cortex for SC cells in situ has not been characterized, with the only reported thickness measurements of 370 nm (Vargas-Pinto et al. 2013) having been

made on cultured cells that were much thicker than the in situ cells used in the current study. More specifically, cultured SC cells had an average nonnuclear thickness of 3 μm (Vargas-Pinto et al. 2013), while the average nonnuclear thickness of the cells examined in situ in the current study was roughly 0.5 μm . Thus, use of a 370-nm cortex in our modeling studies would have essentially converted the entire nonnuclear region of the cell into the cortex. Instead, we assumed a cortex thickness of either 100 or 200 nm based on the values reported for other types of cells (Bray 2001; Clark et al. 2013; Dailey et al. 2009; Deguchi et al. 2009; Fritzsche et al. 2013) and on the minimum cell thicknesses reported in Fig. 2. We recognize that this is an approximation, but it seems reasonable in view of the minimum thickness of the 4 cells studied (~ 300 nm); in particular, the 100- to 200-nm range for the thickness of the cortex is consistent with the maximum thickness the cortex could have while maintaining a uniform distribution along the basal and apical surfaces of the cell.

Note that we did not model the nucleus of the cell as having different material properties compared to nonnuclear regions in the interior of the cell. While other investigators have found the nucleus to be stiffer than the nonnuclear region of cells (Caille et al. 2002), we found no significant difference between these two regions in SC cells (Vargas-Pinto et al. 2013), with AFM results only showing a significant difference between the stiffness of the cortex and that of the internal cytoskeleton. The plasma membrane was assumed to have a negligible effect on cellular deformations due to the small thickness of the lipid bilayer (~ 5 nm, Boal 2002) compared to the thickness of the cell cortex.

2.3 Finite element analysis

The files containing the geometries of SC cells were imported as parts into ABAQUS version 6.11 (Dessault Systemes

Simulia Corp., Providence, RI). Cells were modeled as neo-Hookean materials (Yamada et al. 2010), and in our baseline case, we assumed material parameters $C_{10} = 168 \text{ Pa}$ and $D_1 = 1.2 \times 10^{-4} / \text{Pa}$ for homogeneous cells, corresponding to a Young's modulus (E) of 1 kPa and Poisson's ratio of 0.49 based on the values of SC cell stiffness measured using different techniques (Vargas-Pinto et al. 2013; Zeng et al. 2010; Zhou 2012). Because AFM measurements can differentiate between the stiffness of the cortex and that of the internal cytoskeleton depending on tip geometry (Vargas-Pinto et al. 2013), the modulus for cells with a stiff cortex was based on AFM results. Specifically, for cells modeled as having a stiff cortex, we assumed an aggregate modulus of 0.8 kPa as measured with $10 \mu\text{m}$ spherical tips (Vargas-Pinto et al. 2013). The method used to select the individual values for the stiffness of the cortex (E_{cortex}) and that of the cytoplasm ($E_{\text{cytoplasm}}$) is described in Sect. 2.5.

Cell geometries were discretized using 4-node linear tetrahedral elements, with an average element size of $0.2\text{--}0.3 \mu\text{m}$ as determined through a mesh refinement study. Further reducing the element size by half did not affect our results ($<2\%$ difference in peak strain). A sample image is given in Online Resource 1.

The attachments between the cell and its substrate were modeled by applying a zero displacement constraint to the nodes at the periphery of the basal surface of the cell, and the pressure load was applied to the entire basal surface. For those cases in which the cell cortex was modeled as a separate component, a no-slip condition was defined between the interior surface of the cell cortex and the exterior surface of the cytoplasm. Zero stress was applied to the other surfaces of the cell. The pressure load was increased up to the point of cell failure (see Sect. 2.4), and the resulting stress, strain, and displacement fields were computed as a function of pressure load. Values of strain reported here are the maximum principal values of the logarithmic strain (LE), defined as $\text{LE} = \sum_{i=1}^3 \ln \lambda_i \mathbf{n}_i \mathbf{n}_i^T$, where λ_i are the principal stretches and \mathbf{n}_i the principal stretch directions.

We also carried out tests to ensure that our results were insensitive to the boundary condition used at the periphery of the cell. To do so, we considered the high strain regions (strain greater than 100% in the baseline case) for one cell, and in these regions, prescribed zero displacement on an additional set of nodes, namely those nodes neighboring the cell's edge on its basal surface. For the same pressure loading, constraining these additional nodes caused the peak strain to be reduced from 150% (baseline case) to 149%, showing insensitivity to this boundary condition.

2.4 Criteria for cell mechanical failure

In order to define our criteria for failure, we considered the amount of strain supported by other types of cells. Red blood

cells are known to endure strain levels between 100 and 150% as they deform to pass through narrow channels (Cha et al. 2012), or when deformed using techniques such as controlled cavitation rheology (Li et al. 2013) and optical tweezers (Dao et al. 2003). However, the microstructure of red blood cells is less complex and quite different from that of SC endothelial cells.

The stretch-induced injury model has been widely used to study the effect of strain on other types of cells. The model devised by Ellis et al. (1995) uses a positive pressure to deform an elastic substrate that contains a layer of adherent cells, causing a biaxial stretch of the substrate and of the cells. The amount of strain that cells are subject to is correlated with the bubble-like displacement of the elastic substrate. Cell injury is then quantified using a fluorescent dye that only penetrates injured cells. Using astrocytes, they found increasing number of injured cells for strain levels from 31 to 72%. McKinney et al. (1996) used the same model to study the deformation of a mix of neuronal and glial cells and of bovine aortic endothelial cells. When exposed to strain levels up to 72%, they found the level of injured cells to be similar for astrocytes and the mix of neuronal and glial cells, while aortic endothelial cells were more resistant to injury. To reach the same level of cell injury, endothelial cells needed to be exposed to strain levels up to 180%. Using a similar model, Skotak et al. (2012) reported a sharp decline in the population of live neuroblastoma cells for strain levels higher than 50%, regardless of the strain rate.

The above studies report the average amount of strain measured on the elastic substrate. However, Winston et al. (1989) found the amount of strain experienced by the cell itself to be between 41 and 85% of the average strain of the substrate. This is because the transfer of strain from the substrate to the cell depends not only on cell attachment, but also on cell morphology (Barbee et al. 1994). Thus, using this ratio, injured endothelial cells reported by McKinney et al. would have experienced strain levels between 77 and 153%. Based on the maximum strain levels reported for other types of cells, we assumed that the upper limit for the amount of logarithmic strain that can be supported by SC cells is 150%.

Cells cultured on a flexible substrate experience a relatively uniform strain distribution across the surface of the cell, so that it is suitable to use the average strain to characterize cell injury. In our modeling studies, SC cells were attached on the periphery. When a uniform pressure was applied to the basal surface, the cell itself deformed in a bubble-like shape and the resulting strain was concentrated on the periphery of the cell. We therefore used the peak strain as opposed to the average strain of the cells as the criterion for cell failure, i.e., we took the maximum pressure that cells can support (P_{max}) as that which caused the logarithmic strain to reach 150% anywhere in the cell.

2.5 Estimate values for E_{cortex} and $E_{\text{cytoplasm}}$

Vargas-Pinto et al. (2013) used sharp and spherical AFM tips to show that the modulus of the cortex of SC cells is much higher than that of their internal cytoskeleton. They used a finite element model to determine the modulus that would be obtained from AFM measurements (E_{apparent}) as a function of E_{cortex} and $E_{\text{cytoplasm}}$ when using both sharp and spherical tips. However, the indentation depth with the sharp tip in those finite element studies was limited to 80 nm due to a numerical limitation (Vargas-Pinto et al. 2013), and this prevented them from using AFM data to solve the inverse problem (given E_{apparent} for a sharp and spherical tip, find E_{cortex} and $E_{\text{cytoplasm}}$) since their experimental measurements used indentations 400 nm deep.

We take a different approach here. While values of E_{apparent} measured experimentally with sharp and spherical AFM tips are affected by both cortical and cytoplasmic stiffness, sharp tips probe primarily the cortex and larger spherical tips probe mostly the cytoplasm (Vargas-Pinto et al. 2013). Thus, we consider the value of 6.7 kPa measured by Vargas-Pinto et al. using sharp tips to be a lower bound for the stiffness of the cortex and assumed $E_{\text{cortex}} = 10$ kPa accordingly. Then, given that E_{apparent} was measured as 0.8 kPa for a 10 μm spherical tip (Vargas-Pinto et al. 2013), using $E_{\text{cortex}} = 10$ kPa, the inverse problem can be solved using FEM to find that $E_{\text{cytoplasm}} = 0.3$ kPa (Vargas-Pinto 2014). Thus, in our baseline case, $E_{\text{cortex}}/E_{\text{cytoplasm}}$ was taken to be 33. In addition, we studied cases in which the cortex was taken to be 10 (McGarry and Prendergast 2004) or 100 (Guo et al. 2013) times stiffer than the cytoplasm, i.e., in which $E_{\text{cytoplasm}} = 1$ or 0.1 kPa.

3 Results

We characterized the pressure-induced deformation of SC cells, first by modeling cells as homogeneous materials and then by including a cortex stiffer than the cytoplasm. To characterize cell deformation, we focused on cell displacement and cell thinning because these parameters are associated with the formation of giant vacuoles and pores. The results for homogenous cells are presented first, addressing the influence of cell geometry. Second, we present the results for cells with a cortex, addressing the influences of cortex thickness and cytoplasmic stiffness. Last, we present a brief examination on the influence of cell–substrate attachment.

3.1 Homogeneous SC cells

We studied the deformation of 4 different cells under pressure. The displacement fields just prior to failure (150 % peak strain) are shown in Fig. 3 and the corresponding strain dis-

tributions in Fig. 4. In general, cell displacement tended to reach its maximum value at locations where cells were thin and wide. The cell thickness was determined based on the distance between the basal and apical surfaces of the cell, and the width was determined based on the distance between attachments on opposite sides of the cell.

Because the nucleus (marked as “*” in Fig. 3) was the thickest part of the cell, the deformation in this region was highly reduced. For example, the nucleus of SC01 was located at the center of the cell, causing a decrease in displacement (green color) compared to the sides of the cell where the displacement was higher (red spots). A similar reduction in displacement due to the presence of the cell nucleus can be seen for SC02 and SC04. For SC03, the nucleus was located toward the side where the cell was relatively narrow, which also contributed to the decreased displacement of this region.

For cells SC02, SC03, and SC04, the point of maximum displacement was at the widest part of the cell. For SC01, the widest part of the cell was where the nucleus was located, and thus, the maximum displacement was not exactly at the widest point. For all cells studied, the maximum displacement was at a nonnuclear region where the cell was thin but not necessarily at the point where the cell was thinnest. Comparing Figs. 2 and 3, it can be seen that the thickness at the point of maximum displacement (h in Fig. 3) is greater than the minimum thickness of the cell reported in Fig. 2, for all cells except SC03. This suggests that, although both the width and the thickness of the cell help predict the point of maximum displacement, the width is perhaps more important.

The strain was always highest at the periphery of the cells, where the attachments to the substrate were located (Fig. 4). The location of maximum strain did not necessarily underlie a thin region of the cell. For SC04, the strain was highest at an attachment point where the cell was relatively thick (1 μm) compared to the minimum thickness of the cell (0.4 μm), while for SC03, the strain was highest at an attachment point where the cell was very thin. The maximum strain did not occur at the widest part of the cell either. By comparing the results from Figs. 3 and 4, it can further be seen that the location of maximum strain did not coincide with the location of maximum displacement. When cells reached 150 % strain, the peak stress was located at the attachment sites and ranged between 4.4 and 6.2 $\text{nN}/\mu\text{m}^2$ depending on the cell.

Under physiologic conditions, SC cells experience large deformations in response to the pressure gradient across this endothelium. As a result of this deformation, the cytoplasm becomes very thin, and this thinning has been postulated as being necessary for pore formation (Johnson 2006). We wanted to determine whether such thinning of the cytoplasm also occurred in our simulations. At the highest pressure supported, the thickness of SC03 (thinnest cell) at the point of maximum displacement changed from 0.31 (original) to 0.30 μm (deformed) (3 % decrease), while for SC04 (thick-

Fig. 3 Total displacement (μm) of homogeneous cells when exposed to maximum supportable pressure (P_{max}). The center of the figure shows the views of entire cells ($E = 1 \text{ kPa}$) from the basal surface. Location of the nucleus is indicated by horizontal bar with asterisk. The right side of the figure shows cross sections taken in the vertical direction taken at the location of maximum displacement (arrows) for the deformed geometries (color scale). The undeformed geometries (gray) at point of maximum displacement also included for comparison ($h = \text{cell thickness based on the distance between the basal and apical surfaces at point of maximum displacement, } a = \text{cell width based on the distance between the attachments, shown as arrowheads}$)

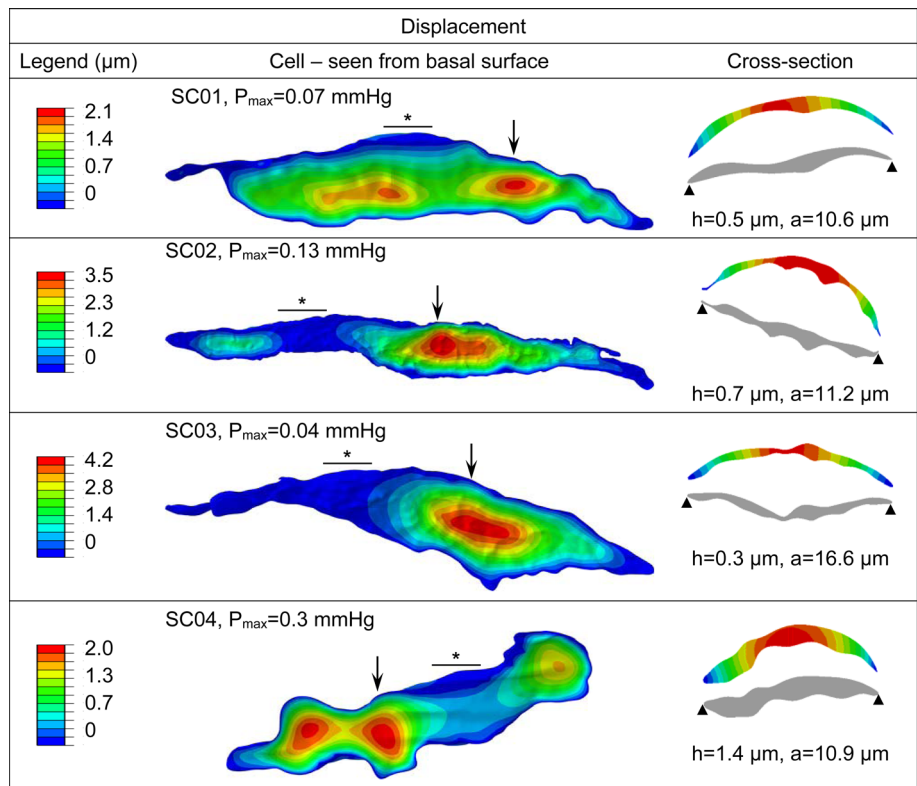


Fig. 4 Strain distribution for homogeneous cells when exposed to maximum supportable pressure (P_{max}). The center of the figure shows views of entire cells ($E = 1 \text{ kPa}$) from the basal surface. The right side of the figure shows cross sections taken in the vertical direction at the location of maximum strain (arrows)

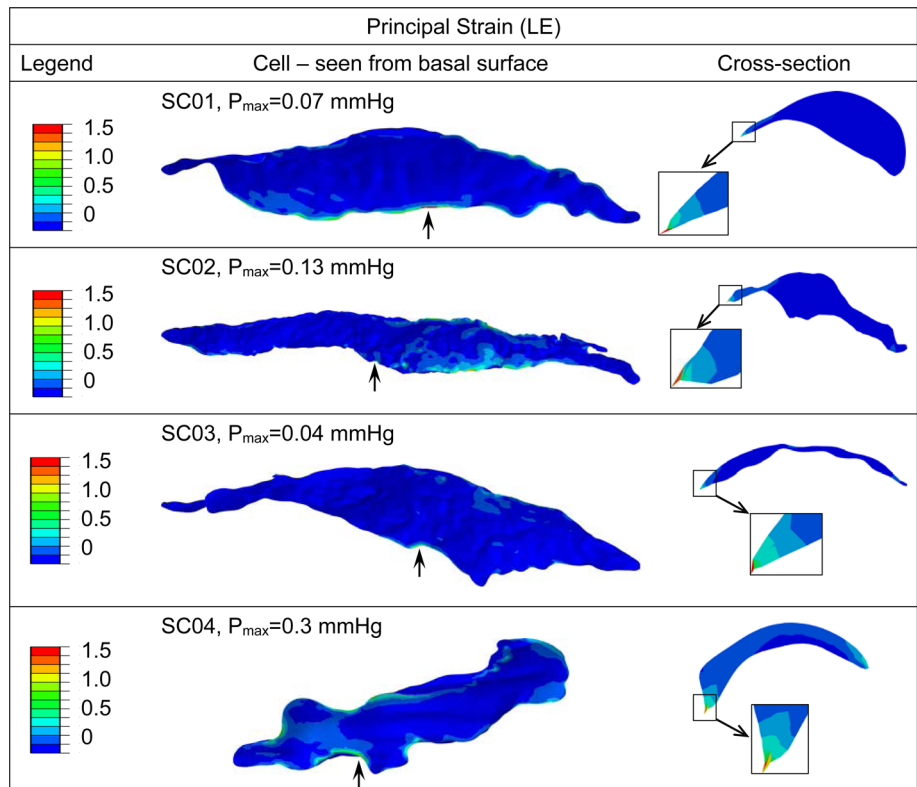


Table 1 Effect of the cell cortex on the biomechanics of cell SC04

	Quantity of interest	Model		
		No cortex (homogeneous)	100-nm cortex	200-nm cortex
Cell thickness measured at point of maximum displacement. $E_{\text{cytoplasm}}$ = cytoplasmic stiffness, E_{cortex} = cortical stiffness, P_{max} = maximum pressure supported by cell	$E_{\text{cytoplasm}}$ (kPa)	0.8	0.3	0.3
	E_{cortex} (kPa)	N/A	10	10
	P_{max} (mmHg)	0.23	1.78	2.36
	Max. Displacement (μm)	1.83	4.48	3.37
	Ratio initial/final thickness	0.90	0.51	0.71
	Displacement (μm) at 0.23 mmHg	1.83	1.01	0.65
	Initial/final thickness at 0.23 mmHg	0.90	0.93	0.97

est cell), the thickness changed from 1.43 to 1.28 μm (10 % decrease). Thus, no substantial cell thinning occurred when cells were modeled as having homogeneous, isotropic material properties.

The results described above were based on a cell modulus of 1 kPa. For the 4 cells studied, the maximum pressures that the cell could tolerate before failure (P_{max}) were 0.07, 0.13, 0.04, and 0.3 mmHg, respectively. Based on this information, we identified SC03 and SC04 as the weakest and strongest (able to support highest pressure) cells, respectively. SC04 was the shortest, thickest, and narrowest cell. SC03 was the widest, with a thickness and length closer to cells SC01 and SC02 (Fig. 2). Thus, from a geometric point of view, our results are self-consistent, i.e., width and thickness help predict not only the weakest and strongest parts of the cell but also the weakest and strongest cells overall.

We verified that increasing the modulus of homogeneous cells caused a similar increase in the maximum pressure supported, such that P_{max}/E remained constant. Thus, changing the modulus from 1 to 10 kPa increased P_{max} by a factor of 10 to values of 0.7 to 3 mmHg, depending on the cell. Decreasing the cell modulus to 0.8 kPa, to match values measured with a 10 μm spherical AFM tip (Vargas-Pinto et al. 2013), resulted in maximum supported pressures even lower than 0.3 mmHg.

3.2 Biomechanical effects of the cell cortex

AFM studies have shown that the cortex of SC cells is stiffer than the internal cytoskeleton (Vargas-Pinto et al. 2013). Having characterized the deformation of SC cells when modeled as homogenous materials, we then investigated the biomechanical effect of the cortex being stiffer than the rest of the cell. SC04 was used for this purpose because it was the strongest cell (was able to support the highest pressure); therefore, results for this cell will suggest an upper bound for the maximum pressure drop that SC cells can support in situ.

The cortical and cytoplasmic stiffness used to study the effect of the cell cortex was chosen such that the aggregate

modulus of the cell with a stiff cortex was equivalent to the modulus used for the homogeneous cell (Sect. 2.5). Table 1 shows that, for an equivalent aggregate modulus, cells with a stiff cortex can support much higher pressures than can homogeneous cells. For example, P_{max} for the cell with a 200-nm cortex (2.4 mmHg) was an order of magnitude higher than that for the homogeneous cell with equivalent stiffness and comparable to P_{max} for a homogeneous cell with a modulus of 10 kPa (3 mmHg). This suggests that the cortex supports most of the pressure load, and the maximum pressure that the cell can support is largely determined by the stiffness of the cell cortex.

Consistent with results for homogeneous cells, cells with a stiff cortex also had their peak strain localized at the periphery where the attachments were located, and the displacements were larger at wide, nonnuclear regions (Fig. 5). The maximum displacement was localized to the same region for both cells with a stiff cortex and the equivalent homogeneous cell. The maximum displacement for cells with a stiff cortex was much higher than that for the homogeneous cell with equivalent stiffness (Table 1). The increased displacement of cells with a cortex led to a much greater reduction in cell thickness at the point of maximum displacement, compared to the homogeneous cell (Figs. 5a c). For cells with a stiff cortex, the ratio of final to initial thickness at the point of maximum displacement varied from 0.5 to 0.7 depending on the thickness of the cortex (Table 1).

It is important to note that comparisons made with respect to the maximum deformation were not made using a constant pressure, but instead using the maximum pressure supportable by each cell, which was higher for cells with a stiff cortex than for the homogeneous cell. Instead, if we chose to compare the deformation when cells were subjected to a constant pressure, the homogeneous cell had a larger displacement and greater cell thinning as compared to cells with a stiff cortex (Table 1). For example, at a pressure of 0.2 mmHg (P_{max} for the homogenous cell), the displacement of the cell with a 100-nm cortex was 45 % smaller than that of the homogeneous cell (Fig. 5a, b).

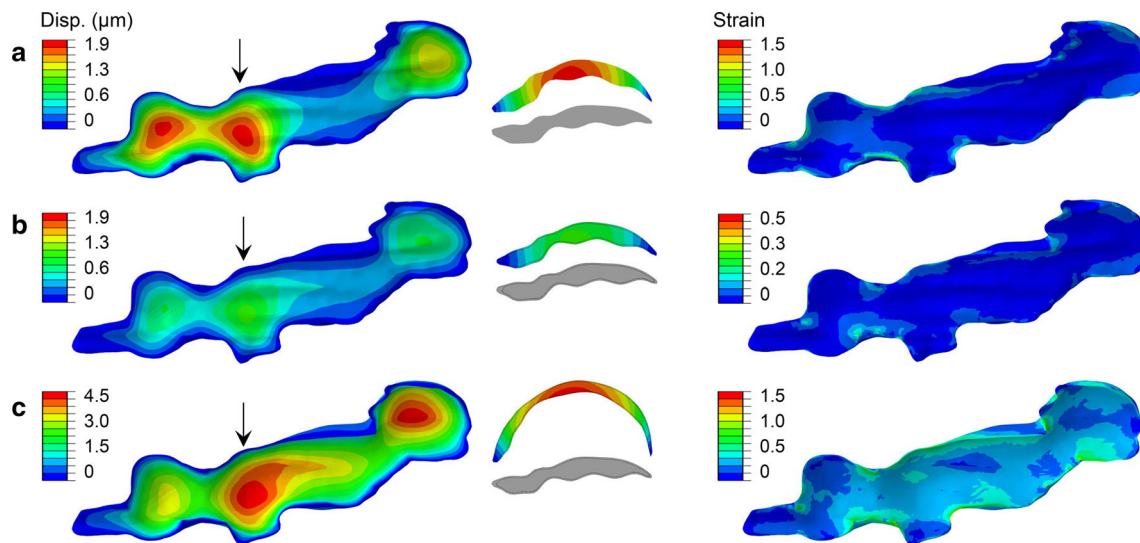


Fig. 5 Effect of the cell cortex on SC cell deformation. Displacement (μm , *left column*) and strain distribution (*right column*) for cell SC04 modeled **a** as homogeneous material ($E = 0.8$ kPa), and **b** as the combination of a 100-nm cortex and cytoplasm ($E_{\text{cortex}} = 10$ kPa, $E_{\text{cytoplasm}} = 0.3$ kPa). Both cells have equivalent stiffness and were subjected to a pressure of 0.2

mmHg. Vertical cross sections (*center*) were taken at location of maximum displacement (*arrows*) to show the geometry of the cell before (*gray*) and after (*colored*) the pressure load is applied. **c** Deformation of cell with a stiff cortex when subjected to the maximum supportable pressure (1.8 mmHg). Note different *color scales*

3.3 Effect of cytoplasmic stiffness

We also examined the effect of cytoplasmic stiffness, while cortex stiffness was held constant. As the cytoplasmic stiffness was increased from 0.1 to 1 kPa, there was a small (for a 200-nm cortex)-to-moderate (100-nm cortex) increase in P_{max} (Table 2). Changes in cytoplasmic stiffness also had a small effect on the strain distribution (Fig. 6). Regardless of the stiffness of the cytoplasm, the strain was always highest at a point where the cell cortex was attached to the substrate, and the cell displacement was highest at central, nonnuclear regions where the cell was widest (Fig. 6).

Changes in cytoplasmic stiffness and cortex thickness affected cell displacement and cell thinning to different extents (Fig. 6). As expected, changes in cell thickness were greater for cells with $E_{\text{cytoplasm}} = 0.1$ kPa compared to $E_{\text{cytoplasm}} = 1$ kPa. For cells subject to a fixed pressure (1.58 mmHg, which is the lowest P_{max} for cells with a cortex, see Table 2), increasing the stiffness of the cytoplasm from 0.1 to 1 kPa decreased the displacement of the cell with a 100-nm cortex by 32% and that with a 200-nm cortex by 21%. The reduction in cell thinning was also more dramatic for the cell with a 100-nm cortex (51%) than that with a 200-nm cortex (27%). Thus, the cell with a 100-nm cortex was more sensitive to changes in cytoplasmic stiffness than that with a 200-nm cortex.

3.4 Effect of cell-to-substrate attachments

In all of the studies described above, we have only considered attachments of the cells at their periphery and neglected the effect of focal adhesions and other cell–substrate attachments. In situ, SC cells form junctions with neighboring cells at their periphery, but also with the underlying basal lamina and with cells in the JCT (Ethier 2002). A complete characterization of the effects of cell-to-substrate attachment size and location is beyond the scope of this study. However, in our efforts to characterize cell deformation as a function of geometry, we found that the deformation and maximum pressure supported by SC cells depend strongly on the width of the cell. Thus, we were interested in determining whether the addition of a cell–substrate attachment (s) near the center of the cell increased the maximum pressure that cells can support by decreasing the “effective width” of the cell.

Toward this end, we considered three cases: (1) adding one (point) attachment at a single finite element node, (2) adding one attachment (1 μm long and 0.8 μm wide comprised of all nodes inside this 0.6 μm^2 hexagonal area) similar in size to focal adhesion complexes (Balaban et al. 2001; Geiger et al. 2001), and (3) adding a total of two attachments the size of the single attachment in (2). For all cases, cell–substrate attachments were added near the center of the cell where the displacement was the greatest prior to the addition of the

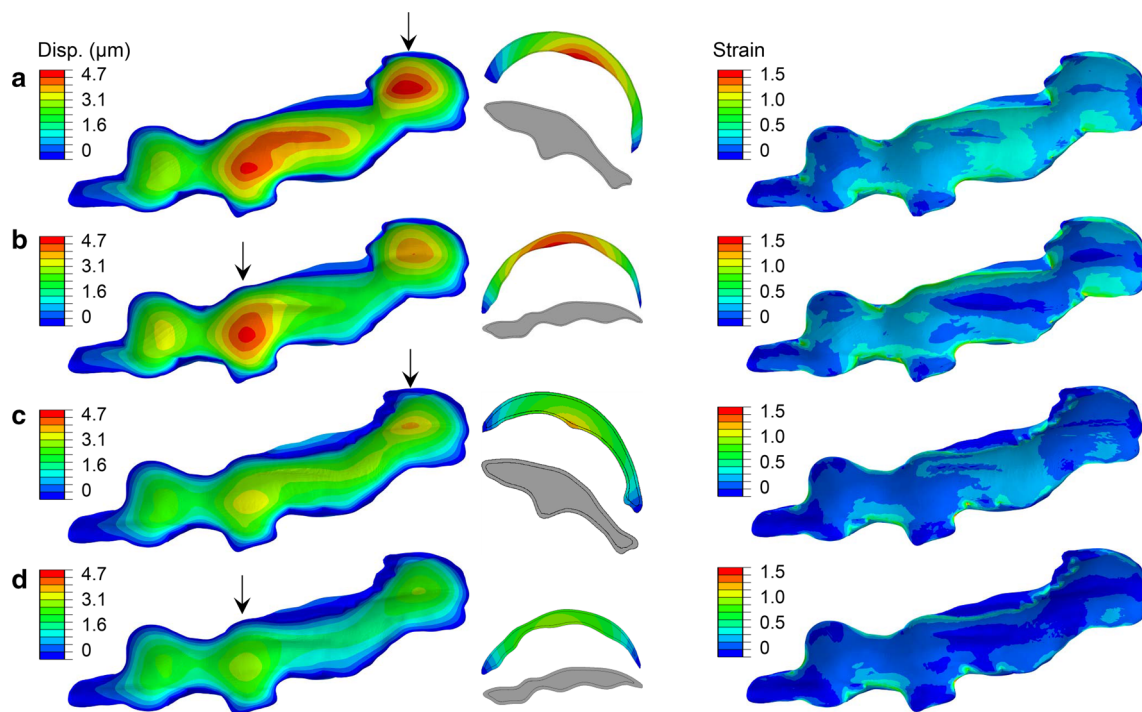


Fig. 6 Effect of cytoplasmic stiffness on the deformation of cell SC04 when the biomechanical effects of the cortex are included. Shown are displacement fields (μm , *left column*) and strain distribution (*right column*) when maximum supportable pressure is applied. Vertical cross sections (*center*) were taken at point of maximum displacement

(*arrows*). **a** 100-nm cortex, $E_{\text{cytoplasm}} = 0.1 \text{ kPa}$, $P_{\text{max}} = 1.6 \text{ mmHg}$, **b** 100-nm cortex, $E_{\text{cytoplasm}} = 1 \text{ kPa}$, $P_{\text{max}} = 2.5 \text{ mmHg}$, **c** 200-nm cortex, $E_{\text{cytoplasm}} = 0.1 \text{ kPa}$, $P_{\text{max}} = 2.3 \text{ mmHg}$, **d** 200-nm cortex, $E_{\text{cytoplasm}} = 1 \text{ kPa}$, $P_{\text{max}} = 2.5 \text{ mmHg}$

Table 2 Effects of changes in cytoplasmic stiffness for SC04 when the biomechanical effects of a stiff cortex (10kPa) were included

Quantity of interest	Cortex thickness			
	100 nm		200 nm	
$E_{\text{cytoplasm}}$ (kPa)	0.1	1	0.1	1
P_{max} (mmHg)	1.58	2.30	2.29	2.48
Max. Displacement (μm)	4.63	4.45	3.62	3.06
Ratio initial/final thickness	0.49	0.58	0.54	0.73
Displacement (μm) at 1.58 mmHg	4.63	3.16	2.77	2.19
Initial/final thickness at 1.58 mmHg	0.49	0.74	0.65	0.83

Cell thickness was measured at the point of maximum displacement. $E_{\text{cytoplasm}}$ = cytoplasmic stiffness, P_{max} = maximum pressure supported by cell

attachment. We chose to study the effect of cell-to-substrate attachments on cell SC03 because it was the widest cell, and thus, we expected the effect of having an additional attachment in the center of the cell to be greater compared to the other 3 cells.

Figure 7 compares the maximum displacement and strain distribution for SC03 subject to the same pressure (0.04 mmHg, which is P_{max} for this cell when modeled as having a homogeneous modulus) but with different attachments. In the baseline case, it was assumed that the cell was only attached at the periphery (Fig. 7a). When a single node near the center of the cell was attached to the substrate, the strain concentrated at that one node exceeded 150% at a

pressure lower than 0.04 mmHg leading the attachment to be lost, and thus, the maximum supportable pressure was not altered compared to the baseline case. When the attachment area was increased to $0.6 \mu\text{m}^2$ (case 2: Fig. 7b) and the pressure was held at 0.04 mmHg to compare to the baseline case, the strain was highest at the additional attachment site (116%). This additional attachment enabled the cell to support up to 0.06 mmHg (a 50% increase compared to baseline case). At that pressure, the strain was again highest at the periphery of the cell (150%) while at the attachment site, it was 144%. Adding a total of two attachment areas at a pressure of 0.04 mmHg (P_{max} for the baseline case) showed a further lowering of the peak strain for the cell to 88%

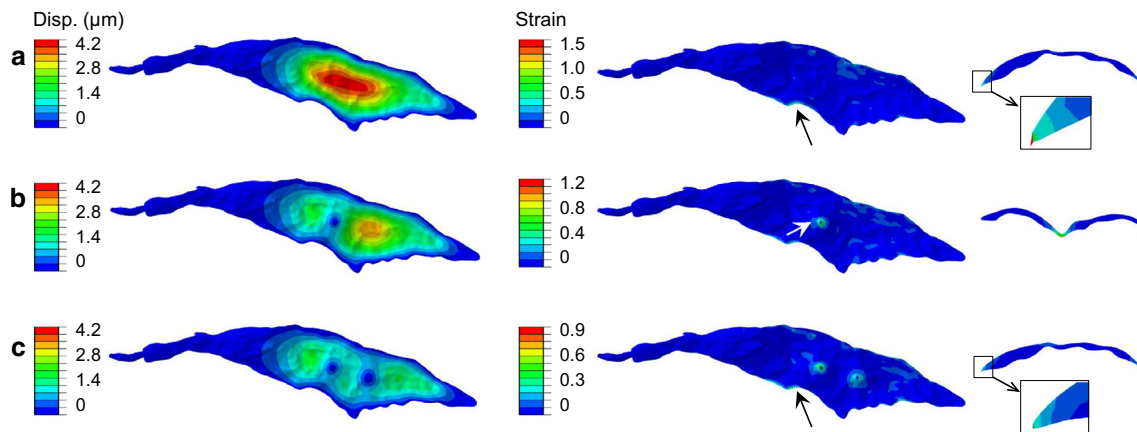


Fig. 7 Effect of cell-to-substrate attachments on the displacement (μm , left column) and strain (right column) of cell SC03 when the applied pressure is 0.04 mmHg. Vertical cross sections were taken at point of maximum strain (arrows). **a** Baseline case, cell attached only

at the periphery, **b** cell attached at the periphery and over a central area of $0.6\mu\text{m}^2$, **c** cell attached at the periphery and over 2 areas, $0.6\mu\text{m}^2$ each. $E = 1\text{ kPa}$ (no cortex) for all cases

(case 3; Fig. 7c) and further increased the maximum pressure supportable by the cell to 0.07 mmHg.

4 Discussion

4.1 Deformation of SC cells

As aqueous humor crosses the inner wall endothelium to enter the SC, a transendothelial pressure gradient is generated. The magnitude of this pressure gradient has not been determined but it is enough to push the SC cells off their basal lamina, creating invaginations in the cells known as giant vacuoles. Giant vacuoles are seen in central locations near the cell nucleus or near the cell border (Alvarado et al. 2004). During giant vacuole formation, the cytoplasm of the cell becomes very thin, a process believed to facilitate the formation of pores that act as paracellular or transcellular channels (Johnson 2006). By reconstructing four SC cells from SBSEM images and modeling their biomechanics, we studied the pressure-induced deformations of SC cells and found them to be larger in regions where cells were wide and thin. In addition, cells whose overall dimensions were wide and thin supported lower pressures compared to thicker and narrower cells. When the biomechanical effects of a stiff cortex were included, cells were able to support higher pressures, resulting in larger deformations prior to failure.

Because cells were constrained to zero displacement only at their periphery, the maximum displacement occurred in the central regions of the cell. In most cases, the site of maximum displacement corresponded to the location where the cell was widest, while the maximum strain was concentrated at the periphery of the cells, where the attachments were located. This is consistent with the speculation that high strains at the periphery of the cell caused by the transcellular pressure drop

may lead to the simplification of tight junctions and facilitate the formation of paracellular pores (Ye et al. 1997). A significant correlation between biomechanical strain and pore formation has been shown for cultured SC cells (Braakman et al. 2014).

In situ, giant vacuoles have diameters of 1–6 μm and are bounded by a very thin layer of cytoplasm (Inomata et al. 1972; Tripathi 1972). The maximum displacement for the homogeneous cells that we modeled ranged from 2 to 4 μm , which is similar to reported dimensions of giant vacuoles (Tripathi 1972). However, the deformation of homogeneous cells in our models was not accompanied by a significant thinning of the cytoplasm, as opposed to the results for cells with a stiff cortex. In addition, while giant vacuoles are commonly seen near the nucleus of SC cells, our results predict limited deformation in the nuclear region. This could be explained by a nonuniform distribution of cell adhesions on the substrate, where cells in situ could have greater density of attachments to their basement membrane near the periphery as compared to the nuclear region (VanderWyst et al. 2011). This is based on the speculation that giant vacuoles form in locations where cells have poor attachments to the underlying tissue (Inomata et al. 1972).

4.2 Effect of the cell cortex

Our finding that strain is concentrated at the periphery of homogeneous cells emphasizes the importance of the cell cortex in supporting load and is consistent with previous experimental work demonstrating that SC cells have a prominent cell cortex (Vargas-Pinto et al. 2013). Cells with a stiff cortex were able to support pressures up to an order of magnitude higher than homogeneous cells with equivalent stiffness. Thus, the maximum pressure supported by cells depends

highly on the stiffness of the cortex, presumably because the maximum strain occurs at the periphery of the cell where the cortex is attached.

When subject to the same pressure loading, cells with a stiff cortex experienced less displacement and less cell thinning compared to the equivalent homogeneous cell. On the other hand, the maximum deformation for cells immediately before failure (at P_{\max}) was greater for cells with a stiff cortex. At this pressure, cells with a cortex experienced a significant thinning of the cytoplasm, which is consistent with the description of cell deformation during giant vacuole formation (Inomata et al. 1972). Thus, results for cells modeled as the combination of a stiff cortex and a less stiff cytoplasm better match the deformations of SC cells seen in situ, compared to the results for homogenous cells.

4.3 Effect of changes in cytoplasmic stiffness

Increasing the cytoplasmic stiffness by an order of magnitude (with cortical stiffness held constant) caused a small/moderate increase in P_{\max} but had little effect on the strain distribution. In terms of cell deformation, increasing the cytoplasmic stiffness reduced both cell displacement and cell thinning. This suggests that cells with increased cytoplasmic stiffness would create smaller giant vacuoles. A reduction in cell thickness is thought to be an important step in the pore formation process because pores are thought to form when the basal and apical surfaces of the membrane fuse together (Johnson 2006). Thus, it would be more difficult for cells with an increased cytoplasmic stiffness to create transcellular pores. These findings may have important implications for understanding the pathogenesis of glaucoma given that glaucomatous SC cells have an increased cytoskeletal stiffness compared to healthy cells (Overby et al. 2014) and glaucomatous eyes have a reduced density of pores (Allingham et al. 1992; Johnson et al. 2002).

4.4 Effect of cell-to-substrate attachments

We studied the effect of cell-to-substrate attachments by first adding a single attachment near the center of the cell. We found there is a minimum area required for the cell–substrate attachment to help the cell support an increased pressure. If the attachment area is too small, the attachment itself fails and the cell would detach from the substrate at that location, with the net effect that the maximum pressure supportable by the cell is unchanged. Using an attachment area similar to that of a focal adhesion complex, with a single attachment, the cell was able to support a pressure 50 % higher than that supported without the attachment. A second attachment increased the maximum supportable pressure by an additional 17 %, showing a diminishing effect of adding focal adhesions.

4.5 Maximum pressure that SC cells can support

In vitro models have been developed in which cultured SC cells are perfused in the basal-to-apical (physiological) direction. Cells in this system were able to support pressures of 4.5–6 mmHg without cell detachment from the substrate or rupture of the plasma membrane (Alvarado et al. 2004; Pedrigi et al. 2011). Here, we calculated the amount of pressure that SC cells can support in situ, if attached to their substrate only at the cell periphery. Assuming a Young's modulus of 1 kPa and a maximum strain of 150 %, none of the cells studied could support a pressure greater than 1 mmHg. This is consistent with previous estimates of the normal pressure drop across the inner wall based on its porosity and pore size (Bill and Svedbergh 1972).

At the time of failure of homogeneous cells, the peak stresses at the adhesion sites ranged from 4.4 to 6.2 nN/ μm^2 . This is comparable to the stress that focal adhesions can support prior to detachment based on the measurements from Balaban et al. (2001), namely 5.5 nN/ μm^2 .

Adding a 10-kPa cortex to the cell significantly increased the amount of pressure that could be supported, but even for the strongest cell, the maximum pressure was still less than 3 mmHg. The estimated pressure gradient across the entire conventional outflow pathway is perhaps 5 mmHg (Freddo and Johnson 2009) in normal eyes but much higher in glaucomatous eyes. In experimental studies, intraocular pressures up to 30 mmHg have been used without damage to the inner wall (Johnstone and Grant 1973). Thus, without multiple cell–substrate attachments distributed across their basal surface, our models suggest that SC cells could only support a small fraction of the pressure drop seen across the conventional outflow pathway in experimental studies and in glaucomatous eyes.

Because our model indicated that SC cells will fail at relatively low pressures (unless there are extensive centrally located attachments, which have not been reported in the literature), our results suggest that the bulk of the pressure drop across the conventional outflow pathway (and the source of the outflow resistance generating it) must be located proximal to the inner wall endothelium of the SC. This is consistent with the funneling hypothesis which proposes that pores in the inner wall of SC act as modulators of the outflow resistance while the bulk of the resistance is generated within the JCT (Overby et al. 2009).

4.6 Limitations

Many of the results presented here are based on the assumption that cells are attached only at their periphery. Adding more attachments on the basal surface of the cell would affect the shape of pressurized cells and the maximum supportable pressure. Currently, our simulations show basal openings that

extend along the entire width of the cell while, in situ, the basal openings of giant vacuoles are very narrow, less than $2.5\ \mu\text{m}$ in diameter (Tripathi 1972). Modeling cells as having multiple cell–substrate attachments spread throughout their basal surface would decrease the size of the basal openings. In addition, preliminary studies to determine the effect of cell-to-substrate attachments in the middle of the cell showed that the maximum pressure that cells can support is significantly increased by these additional attachments (Sect. 3.4). Because the density of focal adhesions in SC cells in situ has not been characterized and such characterization is beyond the scope of this study, we cannot make more conclusive estimates about the maximum pressure that cells can support.

Our results are also based on the assumption that the cell behaves like an isotropic neo-Hookean material and that cell modulus is constant. The neo-Hookean model is frequently used to analyze cells undergoing large deformations (Jean et al. 2005; Slomka and Gefen 2010; Yamada et al. 2010) and that is certainly the case for SC cells. Zeng et al. (2010) used images of giant vacuoles to estimate the modulus of SC cells in situ and found the modulus to increase significantly as a function of pressure load. Thus, it is possible that SC cells become stiffer under physiological loads, which again would enable cells to support pressures significantly higher than those reported here.

While increasing the modulus of the entire cell will increase P_{max} , we do not expect that to be the case if only the modulus of the nucleus is increased with respect to nonnuclear regions of the cell. Because the nucleus is the thickest part of the cell, our results show that the deformation at the nuclear region is already much smaller than that at nonnuclear regions of the cell with the same stiffness. Thus, increasing the stiffness of the cell nucleus will have little effect on our results.

Our definition of cell failure assumes that SC cells cannot support a strain higher than 150%, based on studies using other endothelial cells. To our knowledge, no studies have been conducted to determine the maximum strain level that SC cells can support. Studies characterizing the effect of high strains on SC cell viability are required to unequivocally determine the maximum pressure that these cells can support.

As is true for all numerical analysis, our results are limited by the resolution of the finite element size. As mentioned in the methods section, a mesh convergence study was performed to ensure that our results were mesh-independent. Even if the mesh were underresolved, the simulations would tend to underestimate peak strains, and thus, conclusions based on peak strains exceeding a threshold are relatively conservative.

5 Conclusions

Our results suggest that the maximum pressure that SC cells can support depends sensitively on the strength and density of the attachments between the cell and its substrate. Without significant attachments to the basal lamina and neighboring cells, SC cells could only support a fraction of the entire pressure drop seen across the conventional outflow pathway. This has important implications for the locus as to where the bulk of aqueous outflow pressure drop resides. Further characterization of the effect of strain on SC cell viability and the density of cell–substrate attachments are required to unequivocally determine the maximum pressure that SC cells can support.

Acknowledgments This work was supported by funding from the National Glaucoma Research program of the Bright Focus Foundation, from the Georgia Research Alliance, and from the National Institutes of Health, grants R01 EY019696, EY022634, and T32 EY007128. This research was supported in part through the computational resources provided by the Quest high-performance computing facility at Northwestern University. We thank Renovo Neural Inc., (Cleveland, OH) for the service of SBSEM imaging.

References

- Allingham RR, de Kater AW, Ethier CR, Anderson PJ, Hertzmark E, Epstein DL (1992) The relationship between pore density and outflow facility in human eyes. *Invest Ophthalmol Vis Sci* 33:1661–1669
- Alvarado JA, Betanzos A, Franse-Carman L, Chen J, Gonzalez-Mariscal L (2004) Endothelia of Schlemm's canal and trabecular meshwork: distinct molecular, functional, and anatomic features. *Am J Physiol Cell Physiol* 286:C621–634
- Balaban NQ et al (2001) Force and focal adhesion assembly: a close relationship studied using elastic micropatterned substrates. *Nat Cell Biol* 3:466–472. doi:10.1038/35074532
- Barbee K, Macarak E, Thibault L (1994) Strain measurements in cultured vascular smooth muscle cells subjected to mechanical deformation. *Ann Biomed Eng* 22:14–22. doi:10.1007/bf02368218
- Bill A, Svedbergh B (1972) Scanning electron microscopic studies of the trabecular meshwork and the canal of Schlemm—an attempt to localize the main resistance to outflow of aqueous humor in man. *Acta Ophthalmol* 50:295–320. doi:10.1111/j.1755-3768.1972.tb05954.x
- Boal D (2002) *Mechanics of the cell*. Cambridge University Press, Cambridge
- Braakman ST, Pedrigi RM, Read AT, Smith JA, Stamer WD, Ethier CR, Overby DR (2014) Biomechanical strain as a trigger for pore formation in Schlemm's canal endothelial cells. *Exp Eye Res* 127:224–235. doi:10.1016/j.exer.2014.08.003
- Bray D (2001) Actin and membranes. In: *Cell movements: from molecules to motility*, 2 edn. Garland Publishing, New York, p 81
- Brilakis HS, Johnson DH (2001) Giant vacuole survival time and implications for aqueous humor outflow. *J Glaucoma* 10:277–283
- Caille N, Thoumine O, Tardy Y, Meister JJ (2002) Contribution of the nucleus to the mechanical properties of endothelial cells. *J Biomech* 35:177–187

- Cha S et al (2012) Cell stretching measurement utilizing viscoelastic particle focusing. *Anal Chem* 84:10471–10477. doi:[10.1021/ac302763n](https://doi.org/10.1021/ac302763n)
- Clark AG, Dierkes K, Paluch EK (2013) Monitoring actin cortex thickness in live cells. *Biophys J* 105:570–580. doi:[10.1016/j.bpj.2013.05.057](https://doi.org/10.1016/j.bpj.2013.05.057)
- Dailey HL, Ricles LM, Yalcin HC, Ghadiali SN (2009) Image-based finite element modeling of alveolar epithelial cell injury during airway reopening. *J Appl Physiol* 106:221–232
- Dao M, Lim CT, Suresh S (2003) Mechanics of the human red blood cell deformed by optical tweezers. *J Mech Phys Solids* 51:2259–2280. doi:[10.1016/j.jmps.2003.09.019](https://doi.org/10.1016/j.jmps.2003.09.019)
- Deerinck TJ, Bushong EA, Thor A, Ellisman MH (2010) NCMIR methods for 3D EM: a new protocol for preparation of biological specimens for serial block face scanning electron microscopy. *Microscopy and Microanalysis Meeting*, Portland, OR, 1–5 August 2010. Available at: <http://ncmir.ucsd.edu/sbfsem-protocol.pdf>
- Deguchi S, Fukamachi H, Hashimoto K, Iio K, Tsujioka K (2009) Measurement and finite element modeling of the force balance in the vertical section of adhering vascular endothelial cells. *J Mech Behav Biomed Mater* 2:173–185
- Ellis EF, McKinney JS, Willoughby KA, Liang S, Povlishock JT (1995) A new model for rapid stretch-induced injury of cells in culture: characterization of the model using astrocytes. *J Neurotrauma* 12:325–339
- Ethier CR (2002) The inner wall of Schlemm's canal. *Exp Eye Res* 74:161–172
- Ethier CR, Coloma FM, Sit AJ, Johnson M (1998) Two pore types in the inner-wall endothelium of Schlemm's canal. *Invest Ophthalmol Vis Sci* 39:2041–2048
- Fiala JC (2005) Reconstruct: a free editor for serial section microscopy. *J Microsc* 218:52–61. doi:[10.1111/j.1365-2818.2005.01466.x](https://doi.org/10.1111/j.1365-2818.2005.01466.x)
- Freddo TF, Johnson M (2009) Aqueous humor outflow resistance. In: Civan M (ed) *The eye's aqueous humor*. Elsevier, Amsterdam, pp 161–192
- Fritzsche M, Lewalle A, Duke T, Kruse K, Charras G (2013) Analysis of turnover dynamics of the submembranous actin cortex. *Mol Biol Cell* 24:757–767
- Geiger B, Bershadsky A, Pankov R, Yamada KM (2001) Transmembrane crosstalk between the extracellular matrix-cytoskeleton crosstalk. *Nat Rev Mol Cell Biol* 2:793–805. doi:[10.1038/35099066](https://doi.org/10.1038/35099066)
- Grant WM (1951) Clinical measurements of aqueous outflow. *AMA Arch Ophthalmol* 46:113–131
- Grierson I, Lee WR (1977) Light microscopic quantitation of the endothelial vacuoles in Schlemm's canal. *Am J Ophthalmol* 84:234–246
- Guo M et al (2013) The role of vimentin intermediate filaments in cortical and cytoplasmic mechanics. *Biophys J* 105:1562–1568. doi:[10.1016/j.bpj.2013.08.037](https://doi.org/10.1016/j.bpj.2013.08.037)
- Inomata H, Bill A, Smelser GK (1972) Aqueous humor pathways through the trabecular meshwork and into Schlemm's canal in the cynomolgus monkey (*Macaca irus*). An electron microscopic study. *Am J Ophthalmol* 73:760–789
- Jean RP, Chen CS, Spector AA (2005) Finite-element analysis of the adhesion-cytoskeleton-nucleus mechanotransduction pathway during endothelial cell rounding: axisymmetric model. *J Biomech Eng* 127:594–600
- Johnson M (2006) What controls aqueous humour outflow resistance? *Exp Eye Res* 82:545–557
- Johnson M, Chan D, Read AT, Christensen C, Sit A, Ethier CR (2002) The pore density in the inner wall endothelium of Schlemm's canal of glaucomatous eyes. *Invest Ophthalmol Vis Sci* 43:2950–2955
- Johnson M, Johnson DH, Kamm RD, DeKater AW, Epstein DL (1990) The filtration characteristics of the aqueous outflow system. *Exp Eye Res* 50:407–418
- Johnstone MA, Grant WG (1973) Pressure-dependent changes in structures of the aqueous outflow system of human and monkey eyes. *Am J Ophthalmol* 75:365–383
- Li F, Chan Chon U, Ohl Claus D (2013) Yield strength of human erythrocyte membranes to impulsive stretching. *Biophys J* 105:872–879. doi:[10.1016/j.bpj.2013.06.045](https://doi.org/10.1016/j.bpj.2013.06.045)
- McGarry JG, Prendergast PJ (2004) A three-dimensional finite element model of an adherent eukaryotic cell. *Eur Cells Mater* 7:27–34
- McKinney JS, Willoughby KA, Liang S, Ellis EF (1996) Stretch-induced injury of cultured neuronal, glial, and endothelial cells: effect of polyethylene glycol-conjugated superoxide dismutase. *Stroke* 27:934–940
- Müller-Reichert T, Mancuso J, Lich B, McDonald K (2010) Three-dimensional reconstruction methods for *Caenorhabditis elegans* ultrastructure. *Methods Cell Biol* 96:331–361. doi:[10.1016/s0091-679x\(10\)96015-9](https://doi.org/10.1016/s0091-679x(10)96015-9)
- Overby DR, Stamer WD, Johnson M (2009) The changing paradigm of outflow resistance generation: towards synergistic models of the JCT and inner wall endothelium. *Exp Eye Res* 88:656–670. doi:[10.1016/j.exer.2008.11.033](https://doi.org/10.1016/j.exer.2008.11.033)
- Overby DR et al (2014) Altered mechanobiology of Schlemm's canal endothelial cells in glaucoma. *Proc Nat Acad Sci* 111:13876–13881. doi:[10.1073/pnas.1410602111](https://doi.org/10.1073/pnas.1410602111)
- Pedrigi RM, Simon D, Reed A, Stamer WD, Overby DR (2011) A model of giant vacuole dynamics in human Schlemm's canal endothelial cells. *Exp Eye Res* 92:57–66
- Skotak M, Wang F, Chandra N (2012) An in vitro injury model for SH-SY5Y neuroblastoma cells: effect of strain and strain rate. *J Neurosci Methods* 205:159–168. doi:[10.1016/j.jneumeth.2012.01.001](https://doi.org/10.1016/j.jneumeth.2012.01.001)
- Slomka N, Gefen A (2010) Confocal microscopy-based three-dimensional cell-specific modeling for large deformation analyses in cellular mechanics. *J Biomech* 43:1806–1816. doi:[10.1016/j.jbiomech.2010.02.011](https://doi.org/10.1016/j.jbiomech.2010.02.011)
- Tripathi RC (1972) Aqueous outflow pathway in normal and glaucomatous eyes. *Br J Ophthalmol* 56:157–174
- VanderWyst SS, Perkumas KM, Read AT, Overby DR, Stamer WD (2011) Structural basement membrane components and corresponding integrins in Schlemm's canal endothelia. *Mol Vis* 17:199–209
- Vargas-Pinto R (2014) Increased subcortical stiffness of Schlemm's canal endothelial cells and its role in glaucoma. Northwestern University, Evanston
- Vargas-Pinto R, Gong H, Vahabikashi A, Johnson M (2013) The effect of the endothelial cell cortex on atomic force microscopy measurements. *Biophys J* 105:300–309
- Winston FK, Macarak EJ, Gorfien SF, Thibault LE (1989) A system to reproduce and quantify the biomechanical environment of the cell. *J Appl Physiol* 67:397–405
- Yamada H, Mouri N, Nobuhara S (2010) Three-dimensional morphometry of single endothelial cells with substrate stretching and image-based finite element modeling. *EURASIP J Adv Signal Process* 1–10. doi:[10.1155/2010/616091](https://doi.org/10.1155/2010/616091)
- Ye W, Gong H, Sit A, Johnson M, Freddo TF (1997) Interendothelial junctions in normal human Schlemm's canal respond to changes in pressure. *Invest Ophthalmol Vis Sci* 37:2460–2468
- Zeng D, Juzkiw T, Read AT, Chan DW, Glucksberg MR, Ethier CR, Johnson M (2010) Young's modulus of elasticity of Schlemm's canal endothelial cells. *Biomech Model Mechanobiol* 9:19–33
- Zhou EH et al (2012) Mechanical responsiveness of the endothelial cell of Schlemm's canal: scope, variability and its potential role in controlling aqueous humour outflow. *J R Soc Interface* 9:1144–1155